CHEMISTRY OF MATERIALS

Article

pubs.acs.org/cm

Surfactant-Directed Synthesis of Ternary Nanostructures: Nanocubes, Polyhedrons, Octahedrons, and Nanowires of PtNiFe. Their Shape-Dependent Oxygen Reduction Activity

Shang-Wei Chou,[†,‡] Jing-Jong Shyue,[§,⊥] Chia-Hua Chien,[#] Chia-Chun Chen,*[,#] Yang-Yuan Chen,*[,¶] and Pi-Tai Chou*[,†,‡]

[†]Department of Chemistry, National Taiwan University, Taipei, 10617 Taiwan

[‡]Center for Emerging Material and Advanced Devices, National Taiwan University, Taipei, 10617 Taiwan

[§]Department of Materials Science and Engineering National Taiwan University, Taipei, 10617 Taiwan

[⊥]Research Center for Applied Science, Academia Sinica, Taipei, 11529 Taiwan

[#]Department of Chemistry, National Taiwan Normal University, Taipei, 11677 Taiwan

[¶]Institute of Physics, Academia Sinica, Taipei, 11529 Taiwan

Supporting Information

ABSTRACT: We report a rational method for preparation of ternary alloy (PtNiFe) nanocrystals with various shapes. PtNiFe nanocubes, polyhedrons, and octahedrons are prepared via fine-tuning the alloy compositions and surfactants, so that the crystal facet−surfactant bindings on the growth seed can be well controlled. Nanowires grow in the cylindrical template built via high concentrations of oleylamine. In the electrocatalysis examination, it appears that the oxygen reduction reaction (ORR) activities of all PtNiFe nanostructures outperform that of commercial Pt catalyst in the electrolyte of $HClO_4$ or H_2SO_4. In $HClO_4$, the order of ORR activity is as follows: octahedrons ≈ nanowires > polyhedrons > nanocubes. PtNiFe nanostructures enclosed by a (111) plane, such as octahedrons and nanowires, give the highest ORR activities. Conversely, in H_2SO_4, the ORR activity of PtNiFe nanocubes enclosed by {100} facets is the highest among these nanostructures. The ORR activity increases in the order of nanowires ≈ octahedrons < polyhedrons, establishing a shape dependency in the ORR activity, which is valuable upon performing nanocatalysis in fuel cells.

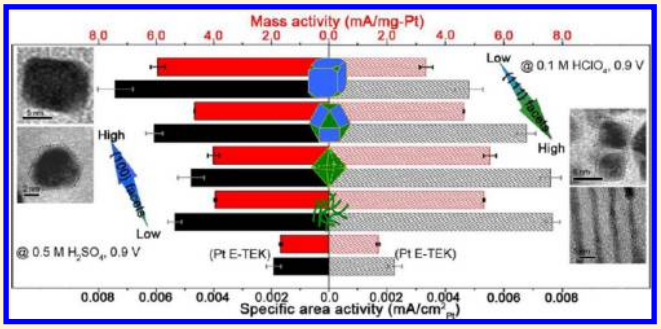

KEYWORDS: *PtNiFe, shape control, nanocube, octahedron, polyhedron, nanowire, oxygen reduction*

INTRODUCTION

Developing an environmentally friendly power source is a challenging task. In this regard, several power sources with low environmental pollution have been sought and intensively investigated. One promising alternative is the fuel cell, a class which mainly includes the proton-exchange membrane fuel cell (PEMFC) and the direct methanol fuel cell (DMFC).[1] However, the slow rate of oxygen reduction reaction (ORR) in the cathode and the high cost of Pt catalysts pose a limitation in practical applications.[2] Design of more efficient and economical catalysts superior to the traditionally carbon-supported Pt (Pt/C) catalyst is thus needed.

Many studies have pointed out that employing Pt-based alloy, intermixing two or more 3d-transition metals, for example, PtFe, PtNi, PtCo, PtPd, and PtNiFe, may attain ORR activity higher than that of the Pt/C catalyst.[3] It is generally accepted that the alloying processes of Pt catalysts involve (1) the easily dissociative absorption of O_2 because of a shortening of Pt−Pt interatomic distances[4a−c] and (2) the decrease of absorbed OH species on the active Pt sites due to a more favorable chemisoption of the OH species onto the sites of transition metals.[4b−d] Moreover, the relationship between ORR activity and chemical composition is addressed from the viewpoint of electronic states of Pt-based alloy catalysts.[5] Recent works have pointed out that the increase in d-band vacancy and the downshift of the d-band center resulted in a decrease in the adsorption strength of oxygenated species and the acceleration of reaction rate in electroreduction.

On the other hand, the difference in Pt-based alloy nanostructures influences catalytic activity per se due to the specific crystallographic planes.[6] Fang et al. have studied the shape control of PtNi nanocrystals through the metal−carbonyl-assistant method[7] and reported that the ORR mass activity (MA) and specific area activity (SA) of PtNi

Received: April 3, 2012
Revised: June 12, 2012
Published: June 15, 2012

octahedrons (the {111}-facet-terminated facets) are 2.8 fold and 5.1 fold, respectively, higher than those of PtNi nanocubes (the {100}-facet-terminated facets) in $HClO_4$.[7b] Yang's group researched the shape control of Pt-based alloy by using the GRAIL (gas reducing agent in liquid solution) approach.[8] Their results showed that PtNi octahedrons and nanocubes had better performance in MA and SA and thus were more active than Pt/C catalyst. Also, both MA and SA increased with the change of shape from nanocube to octahedron in $HClO_4$.

To achieve a shape-dependent alloy nanostructure, solution-phase synthesis is preferable for controlling the compositions and shapes of Pt-based alloy nanocrystals. Generally, the organometallic complexes have been used as precursors for preparations of alloy nanocrystals with different chemical compositions in high-boiling solvent.[6−8] The selection of surfactant molecule in this method so far has been largely based on the adjustment of specific crystal facet−surfactant bindings.[9] Nevertheless, it becomes a very challenging task to prepare ternary alloy with different shapes in a systematic manner due to the complicated atomic ordering degree of the alloy.[10] Herein, we report a rational synthesis, in which the crystal facet−surfactant bindings are delicately tuned through controlling the alloy compositions in combinatorial surfactants, to achieve this goal. We successfully prepare nanocatalysts enclosed by {111} and/or {100} facets, such as nanocubes, octahedrons, polyhedrons, and nanowires, in the ternary alloy (PtNiFe) system. ORR MA and SA of all as-prepared PtNiFe nanostructures outperform those of commercial Pt/C catalyst in different electrolytes (H_2SO_4 and $HClO_4$). Further electrocatalysis examination clearly exhibits the shape-sensitivity of these PtNiFe nanostructures in terms of the ORR activities.

EXPERIMENTAL SECTION

Materials. Platinum acetylacetonate ($Pt(acac)_2$, Acros, 97%), nickel acetylacetonate ($Ni(acac)_2$, Acros, 97%), iron pentacarbonyl ($Fe(CO)_5$, Acros, 99.9%), 1,2-hexadecanediol (HDD, Aldrich, 90%), octadecylphosphonic acid (ODPA, Alfa Aesar, 98%), tri-*n*-octylamine (TOA, Acros, 98%), oleylamine (OLA, Acros, 80−90%), oleic acid (OA, Aldrich, 90%), 1-octadecene (ODE, ACROS, 90%), and nafion solution (Aldrich, 5 wt % in a mixture of lower aliphatic alcohols and water).

Synthesis of PtNiFe Nanocubes. $Pt(acac)_2$ (100 mg), $Ni(acac)_2$ (33 mg), $Fe(CO)_5$ (33 μL), HDD (600 mg), ODPA (220 mg), and OLA (600 μL) were added into a three-neck flask and mixed with ODE (6 mL). Under N_2 gas purge, the reaction mixture was heated to 240 °C at a heating rate of ∼15 °C/min and refluxed for 120 min; afterward, the reaction mixture was cooled to room temperature. In the typical procedure of sample collection, the black product was precipitated by adding ethanol (30−50 mL), which was used as antisolvent, and then separated by centrifugation at 3500 rpm. The final product was stored in hexane.

Synthesis of PtNiFe Octahedrons. $Pt(acac)_2$ (78 mg), $Ni(acac)_2$ (64 mg), $Fe(CO)_5$ (33 μL), HDD (400 mg), TOA (8 mL), and OA (4 mL) were mixed with ODE (6 mL) in a three-neck flask. The manipulation of reaction and collection was the same as that described in Synthesis of PtNiFe Nanocubes except that the reaction time was optimized to 40 min.

Synthesis of PtNiFe Polyhedrons. The reaction mixture included $Pt(acac)_2$ (100 mg), $Ni(acac)_2$ (33 mg), $Fe(CO)_5$ (33 μL), HDD (400 mg), TOA (4 mL), OA (2 mL), and ODE (6 mL). The procedure was the same as that described in Synthesis of PtNiFe Nanocubes except that the reaction time was changed to 40 min.

Synthesis of PtNiFe Nanowires. $Pt(acac)_2$ (100 mg), $Ni(acac)_2$ (33 mg), $Fe(CO)_5$ (33 μL), HDD (400 mg), OLA (10 mL), and ODE (6 mL) were loaded into a three-neck flask. The procedure was the same as that described for Synthesis of PtNiFe Nanocubes except for the reaction time which was changed to 40 min.

Characterization. The low-resolution transmission electron microscopy (TEM) images were obtained with a JEOL J1230 transmission electron microscope at an accelerating voltage of 100 kV. A Philips/FEI Tecnai 20 G2 S-Twin transmission electron microscope was used for high-resolution TEM (HRTEM) images. A drop of sample dispersed in toluene was deposited on a carbon-membrane-coated copper grid (200 mesh). The compositional analysis was carried out with an X-ray energy-dispersive spectrometer on a Philips/FEI Tecnai 20 G2 S-Twin transmission electron microscope. EELS (electron energy loss spectroscopy) maps were obtained with a postcolumn energy filter (Tridium, Gatan) on a JEOL JEM-2100F. Two 60 eV energy windows in front of the Pt $N_{2,3}$, Fe $L_{2,3}$, and Ni $L_{2,3}$ edge were used for background extrapolation with a power function. The background is then subtracted from the 60 eV postedge image. The resultant intensity of the red, green, and blue pseudocolor overlay represents the relative amount of Pt, Ni, and Fe, respectively. The powder X-ray diffraction scan was recorded by PANalytical X' Pert PRO diffractometer. The powder of PtNiFe nanocrystals was placed on the silicon wafer, and the workup procedure was carried out with Cu Kα radiation (wavelength = 1.54178 Å).

Preparation of Carbon-Supported PtNiFe Nanocatalysts. In a typical protocol, carbon black (Vulcan XC-72) was dispersed in *n*-hexane by sonication for 2−3 h. The as-prepared PtNiFe nanocrystals were loaded into the above dispersion at the nanocrystal-to-carbon weight ratio of 20:80, and then this mixture was sonicated for overnight. The resultant samples were collected by centrifugation at 3500 rpm and dried under vacuum conditions. Before the electrochemical measurements, the powder of the nanocatalyst was exposed to UV light and ozone for ∼8 h. The surfactant molecules on the crystal surface were removed by UV−ozone (UVO) treatment. The UVO treatment was performed on a homemade UVO instrument composed of a UV lamp (wavelength = 254 nm, output = 110 mW/cm) and ozone generator (flow rate = 500 mg/h).

Electrochemical Measurements. The electrochemical measurements were carried out with a three-electrode system on an electrochemical workstation (Metrohm Autolab, PGSTAT 100). The saturated calomel electrode was the reference electrode, and a platinum electrode (CH Instruments) was the counter electrode. The working electrode was a glassy carbon rotating disk electrode (RDE, 0.196 cm^2 in area). The RDE was polished with Al_2O_3 powder (CH Instruments, 0.05 μm) and rinsed with deionized water (DI water) before measurements. The solution of 0.1 M $HClO_4$ or 0.5 M H_2SO_4 was used as the supporting electrolyte. All solution was deaerated with N_2 for at least 20 min before measurements. For the preparation of the working electrode, PtNiFe nanocatalyst was dispersed in ethanol through sonication, followed by drop-casting a predetermined amount of PtNiFe nanocatalyst on RDE. After evaporation of the ethanol, 2 μL of the nafion solution was drop-cast onto the glassy carbon surface with the the PtNiFe nanocatalyst. The rate of RDE was set at 1600 rpm for all measurements. The cyclic voltammetry (CV) was carried out in the supporting electrolyte and N_2 purge for 30 cycles to further clean the nanocatalyst surface. The potential was swept between 0 and 1.2 V (vs normal hydrogen electrode, NHE) at a rate of 100 mV/s in CV. The active surface area was determined by the hydrogen desorption in the range of 0.05−0.4 V and assuming 210 μC/cm^2 for a monolayer of adsorbed hydrogen on the Pt surface. The measurements of the oxygen reduction reaction (ORR) were performed in the O_2-saturated electrolyte and O_2 gas flow and at a sweeping rate of 5 mV/s. The rate of RDE was set at 1600 rpm for the ORR measurements. The stability test was performed by cycling the potential between 0 and 1.2 V (vs NHE) in O_2-saturated 0.5 M H_2SO_4 at a scan rate of 100 mV/s

RESULTS AND DISCUSSION

Ternary nanocrystals were synthesized using $Pt(acac)_2$, $Ni(acac)_2$, and $Fe(CO)_5$ as precursors in the presence of a combination of surfactant molecules. Figure 1a and Figure S1

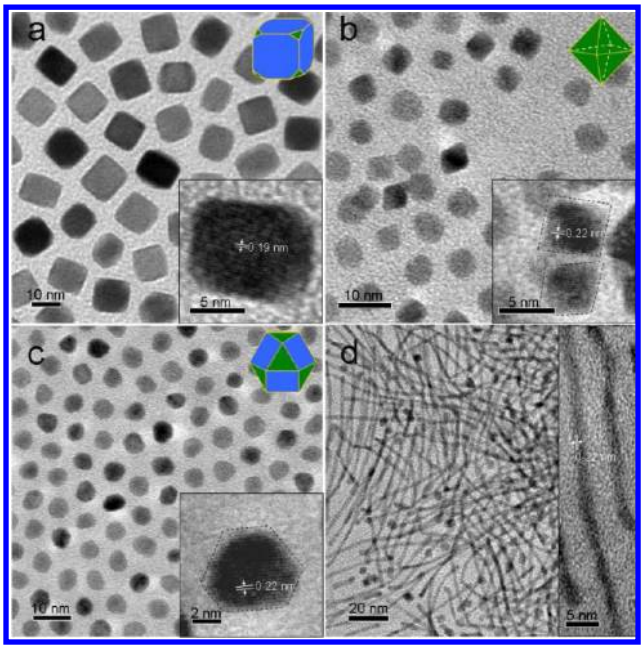

Figure 1. The TEM and HRTEM image of PtNiFe nanostructures, including (a) nanocubes, (b) octahedrons, (c) polyhedrons, and (d) nanowires. The graphic representation shows the three-dimensional image of nanocubes, octahedrons, and polyhedrons. Blue and green represent the {100} and {111} facets, respectively.

(Supporting Information) show the PtNiFe nanocubes obtained in the presence of ODPA and OLA. The average edge length of the PtNiFe nanocube is 11.60 ± 1.49 nm (Figure S1). The inset of Figure 1a clearly shows the spacing distance (~0.19 nm), which is close to the lattice distance of the (200) facet of Pt-based alloy, such as FePt (0.1935 nm, JCPDS card no. 29-0717) and PtNi nanocubes (~0.190 nm).[8] The alloying composition confirmed with an X-ray energy-dispersive spectrometer (EDS) is Pt:Ni:Fe = 79:11:10 (see Supporting Information). Alternatively, TOA and OA are employed to prepare other PtNiFe nanostructures as seen in Figure 1b and 1c. Figure 1b and Figure S2 (Supporting Information) show the octahedron with an average length of 6.95 ± 0.67 nm. The HRTEM image in the inset of Figure 1b shows lattice fringes corresponding to a spacing distance of ~0.22 nm. The spacing distance is close to the lattice distance of the (111) facet of Pt-based alloy, such as FePt (0.2235 nm, JCPDS card no. 29-0717) and PtNi octahedrons (~0.223 nm).[7b] The alloying composition is detected to be Pt:Ni:Fe = 63:27:10.

Figure 1c and Figure S3 (Supporting Information) show a faceted structure mainly having a polyhedral projection; thus, the resultant nanocrystal is named PtNiFe polyhedron. The size distribution of PtNiFe polyhedrons obtained from 100 particles is 6.14 ± 0.44 nm (Figure S3). The HRTEM image in Figure 1c exhibits a spacing distance of 0.22 nm, which is close to the lattice distance of the (111) facet of Pt-based alloy. The alloying composition of polyhedrons is Pt:Ni:Fe = 67:15:18. PtNiFe nanowires were observed when OLA served as a sole capping surfactant. In fact, the product contained both PtNiFe nanoparticles and nanowires (Figure S4a, Supporting Information). However, a large amount of nanoparticles could be removed through the separation method as described by Liu et al.[11] Figure 1d and Figure S4b show the resultant sample after separation. The HRTEM image shows the main interplanar distance to be ~0.22 nm, which is close to the lattice distance of the (111) plane of the Pt-based alloy. The alloying composition of the as-prepared nanowire is Pt:Ni:Fe = 34:20:46.

The powder X-ray diffraction (XRD) scans (Figure 2) exhibit the strongest peaks of the (111) and (200) plane. The

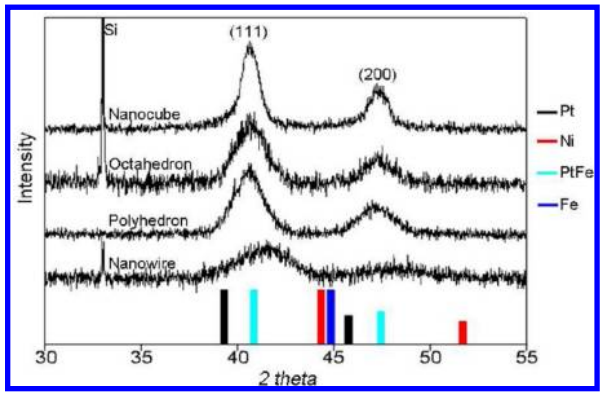

Figure 2. The XRD scans of different PtNiFe nanostructures. For comparison, the patterns of Pt, Ni, PtFe, and Fe serve as reference. Note: the Si signal is from the sample holder.

associated patterns indicate that all PtNiFe nanostructures have chemically disordered structure.[6−8] Through careful examination of the peak positions of Pt, the high-angle shift of PtNiFe nanostructures also reveals that 3d-transition metal atoms are mixed with Pt atoms in these nanostructures.[7,8,9b] Comparing the (111) and (200) pattern shift among various PtNiFe nanostructures, we observed the largest shift in the PtNiFe nanowires due to the lowest Pt-to-M alloying ratio (M: the total amount of Ni and Fe). The alloying composition-based shift is consistent with Vegard's law; that is, the higher amount of 3d-transition metals leads to the high-angle shift of XRD patterns away from that of Pt.[3e,6,8,9b] The full width at half-maximum (fwhm) of the diffraction peaks of PtNiFe nanocubes is the narrowest among these PtNiFe nanostructures. According to Scherrer's equation, there exists a correlation between the fwhm of a pattern of samples and their average sizes observed from TEM images.[12] In particular, the broader peaks of nanowires result from a small diameter of the nanowires.[13] Furthermore, the intensity (I) of XRD patterns also provides rough evidence of the preferred orientation of PtNiFe nanocrystals.[7,8] The intensity ratio of $I_{(111)}/I_{(200)}$ is on the order of nanowires (3.21) > octahedrons (2.59) > polyhedrons (2.39) > nanocubes (2.13), consistent with the morphologies of the resultant nanocrystals. To further probe the composition of the as-prepared ternary alloy, the electron spectroscopic image (ESI) based on electron energy loss spectrometry (EELS) has been performed. The results with RGB pseudocolor (Figure 3a−d; Figure S6 of Supporting Information) clearly reveal the presence of Pt (red), Ni (green), and Fe (blue) elements in each individual PtNiFe nanostructure. Moreover, the corresponding elemental maps show that all nanostructures are composed of random arrangements of Pt, Ni, and Fe elements. Also, HRTEM reveals that all samples are crystalline and there is no amorphous phase present. According to the results of HRTEM, XRD, and EELS maps, it is evident that the Ni and Fe are distributed randomly in the structure of Pt as a solid solution.

During the formation of nanostructures, the alloyed growth seeds are generally formed at an early stage, which are enclosed

dx.doi.org/10.1021/cm301039a | Chem. Mater. 2012, 24, 2527−2533

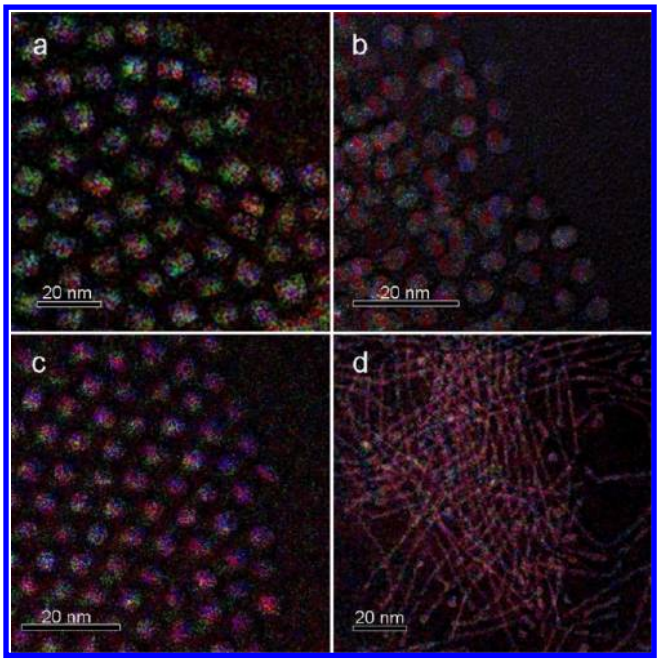

Figure 3. Electron spectroscopic images (ESI) of PtNiFe nanostructures, including (a) nanocubes, (b) octahedrons, (c) polyhedrons, and (d) nanowires. The intensity of the red, green, and blue pseudocolor overlay represents the relative amount of Pt, Ni, and Fe, respectively, obtained with three-window background subtraction.

by several {111} and {100} facets to minimize the total surface energy.[6d,9b,14] Thus, the control of growth rate of these facets on the seeds is a dominant factor in the formation of nanostructure,[9,15] and the growth rate of crystal facets is proportional to the surface energy of crystal facets. Both theoretical and experimental studies point out that the strong surfactant–facet bindings can sufficiently slow the growth rate of crystal facets due to the significant decrease of surface energy of the crystal facets.[9,15b,16] As a result, the controls of specific surfactant–facet bindings on the surfaces of growth seeds depend on the selective surfactant coverage onto the particular facets.[9,16,17] According to a number of theoretical and experimental studies,[15−17] the change in surfactant–facet binding plays a key role in shape control. However, the surfactant–facet binding discussed in those studies has been simplified; for example, one molecule versus one metal surface or one molecule versus bimetal surface. As for the trimetallic alloy system presented in this study, the specific bindings between surfactants and crystal facets are manifolds due to the complicated atomic ordering degrees on their surface. Nevertheless, based on profound experiences and knowledge in shape control of bimetallic systems,[6−8,9b] it is reasonable to propose that the control of surfactant–facet binding via the adjustment of surfactant combination and surface composition is a feasible strategy for the shape control of ternary alloy. We then made great effort to choose the surfactant combinations with different functional groups, for example, TOA vs OA, and ODPA vs OLA, to achieve the optimal control of surfactant–facet binding on the growth seed.

Scheme 1 shows the different ratios (R) of the growth rate for the {111} versus that for {100} facets. The growth ratios are changed by the specific bindings between the surfactant molecules and crystal surfaces, which is the key for shape control of the PtNiFe nanocrystals. For example, the higher surfactant coverage on the {100} facets causes the decrease in

Scheme 1. Formation of Different Nanostructures through Specific Surfactant–Facet Bindings[a]

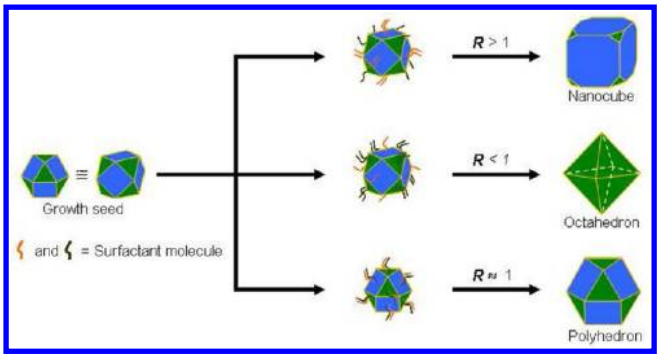

[a]Blue and green represent the {100} and {111} facets, respectively. R: the ratio of the growth rate of {111} facets to that of {100} facets.

growth rate of {100} facets on the seed. The slower growth rate of {100} facets (the R value is larger than 1) results in the formation of nanocubes.[15] In stark contrast, the higher surfactant coverage on {111} facets leads to the slower growth rate of {111} facets (the R value is smaller than 1), rendering octahedral structures.[15] As expected, due to the similar surfactant coverage on various facets, comparable growth rates on {111} facets and {100} facets (R value is 1) lead to the formation of polyhedrons.[9b,15] The growth mechanism of PtNiFe nanowires is proposed to be the same as the formation of FePt nanorods and nanowires due to the fact that the elongated nuclei are clearly observed (see Figure S4b). The high concentration of OLA leads to the formation of cylindrical template inorganic solvent,[13] and OLA serves as the capping surfactants, which cover the different crystal facets of elongated nuclei with different packing densities. Elongated growth in the [100] direction thus results from less density of OLA molecules on the terminus of nuclei.

As compared with commercial Pt/C catalyst, the as-prepared PtNiFe nanostructures are loaded into carbon black at a nanocrystal-to-carbon weight ratio of 20:80 through the procedure described in Supporting Information. Figure 4 reveals the dispersity of carbon-supported nanocatalysts shown by the TEM images. Prior to the electrochemical measurements, these nanocatalysts are exposed to UV light and ozone for 8 h. The surfactant capped on the crystal surface can be removed by UV–ozone (UVO) treatment.[18] Figure S7 (Supporting Information) shows the cyclic voltammetry (CV) of the nanocatalyst (PtNiFe nanocubes supported on carbon black) before and after UVO treatment. Obviously, there is no signal of hydrogen desorption/absorption in the region of 0.05–0.4 V before UVO treatment due to the surfactant coverage on the active surface of the nanocatalyst.[19]

Figure 5a shows CV for the commercial Pt catalyst (Pt E-TEK, black) and all PtNiFe nanocatalysts in 0.1 M $HClO_4$ at room temperature. The important parameter, i.e., "active surface area", of catalysts is then evaluated via the integrated area in the region of hydrogen desorption between 0.05 and 0.4 V. The calculated results, including hydrogen desorption area, electric charge, active area, and specific area, are summarized in Table S1. Figure 5b reveals a characteristic set of polarization curves for the ORR performed in O_2-saturated 0.1 M $HClO_4$ at a scan rate of 5 mV/s. Obviously, the polarization curves (Figure 5b) reveal that the onset potentials of all PtNiFe

dx.doi.org/10.1021/cm301039a | Chem. Mater. 2012, 24, 2527–2533

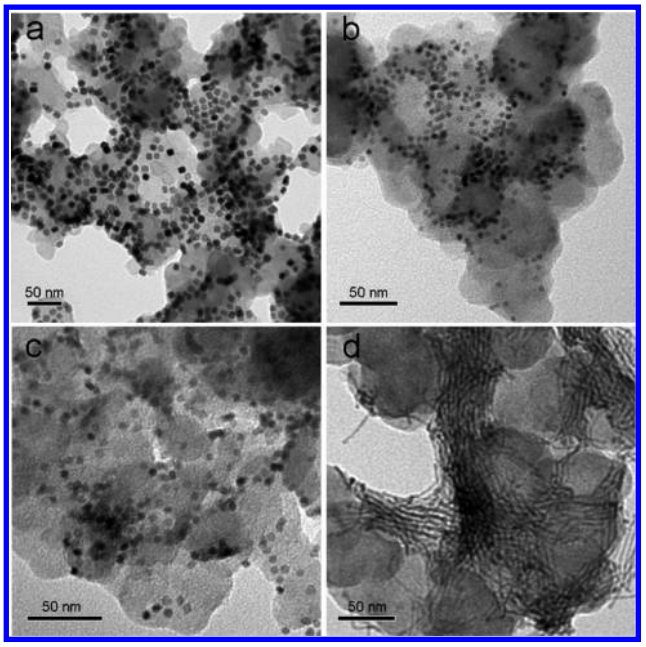

Figure 4. TEM images of PtNiFe nanostructures supported on carbon black, including (a) nanocubes, (b) polyhedrons, (c) octahedrons, and (d) nanowires.

nanocrystals are more positive than that of Pt E-TEK in the mixed kinetic–diffusion control region of 0.8–1.0 V.

Figure 5c depicts the kinetic current densities (at 0.9 V) normalized to the effective Pt mass. The ORR MA for all samples is in the following sequence: octahedrons (5.53 ± 0.22 mA/mg-Pt) > nanowires (5.32 ± 0.03 mA/mg-Pt) > polyhedrons (4.64 ± 0.022 mA/mg-Pt) > nanocubes (3.35 ± 0.228 mA/mg-Pt) > Pt E-TEK (1.71 ± 0.056 mA/mg-Pt). Accordingly, the calculated SA for all type of catalysts are in the following sequence: nanowires (0.0077 ± 0.00026 mA/cm$^2_{Pt}$) > octahedrons (0.0075 ± 0.00036 mA/cm$^2_{Pt}$) > polyhedrons (0.0068 ± 0.00032 mA/cm$^2_{Pt}$) > nanocubes (0.0048 ± 0.00048 mA/cm$^2_{Pt}$) > Pt E-TEK (0.0022 ± 0.00025 mA/cm$^2_{Pt}$). The results indicate that the ORR activities of all PtNiFe nanostructures outperform those of Pt E-TEK. Although the effect of multimetallic Pt-based alloy (intermixing two or more 3d-transition metals) in ORR is not as clear as the effect of bimetallic Pt-based alloy,[3−5] it is generally accepted that the intermixing of 3d-transition metals is capable of altering both Pt–Pt interatomic structure and electronic state.[3] As a result, the enhanced activities could be observed during ORR for the titled ternary systems. Moreover, the difference of ORR activities between polyhedron and octahedron, which have similar alloying composition (Pt-to-M ratio) and size, should directly correlate with their shapes. On the basis of TEM images and the $I_{(111)}/I_{(200)}$ ratios from XRD scans, the exposure of the (111) plane of octahedrons is higher than that of polyhedrons. As expected, higher ORR activities of PtNiFe octahedrons were observed in $HClO_4$.[6d,7b,8] Furthermore, the ORR activity of nanowires is 3–3.5-fold more than that of the commercial Pt catalyst. In particular, the alloying composition of nanowires exhibits the lowest Pt-to-M ratio. Generally, the relation between the ORR activity and the composition of bimetallic Pt-based alloy nanocatalysts can be obtained via a volcano-shaped plot. The bimetallic Pt-based alloy nanocatalysts with alloying composition of 50:50 have the highest ORR activity and are located at the top of the volcano-shaped plot. On the other hand, too much or too little Pt content in the bimetallic Pt-based alloy nanocatalysts leads to a decrease in ORR activity, located at the bottom of the two ends of the volcano-shaped plot.[3a,h,5b] Note that the ORR enhancement of nanowires with the lowest Pt-to-M ratio is similar to that of

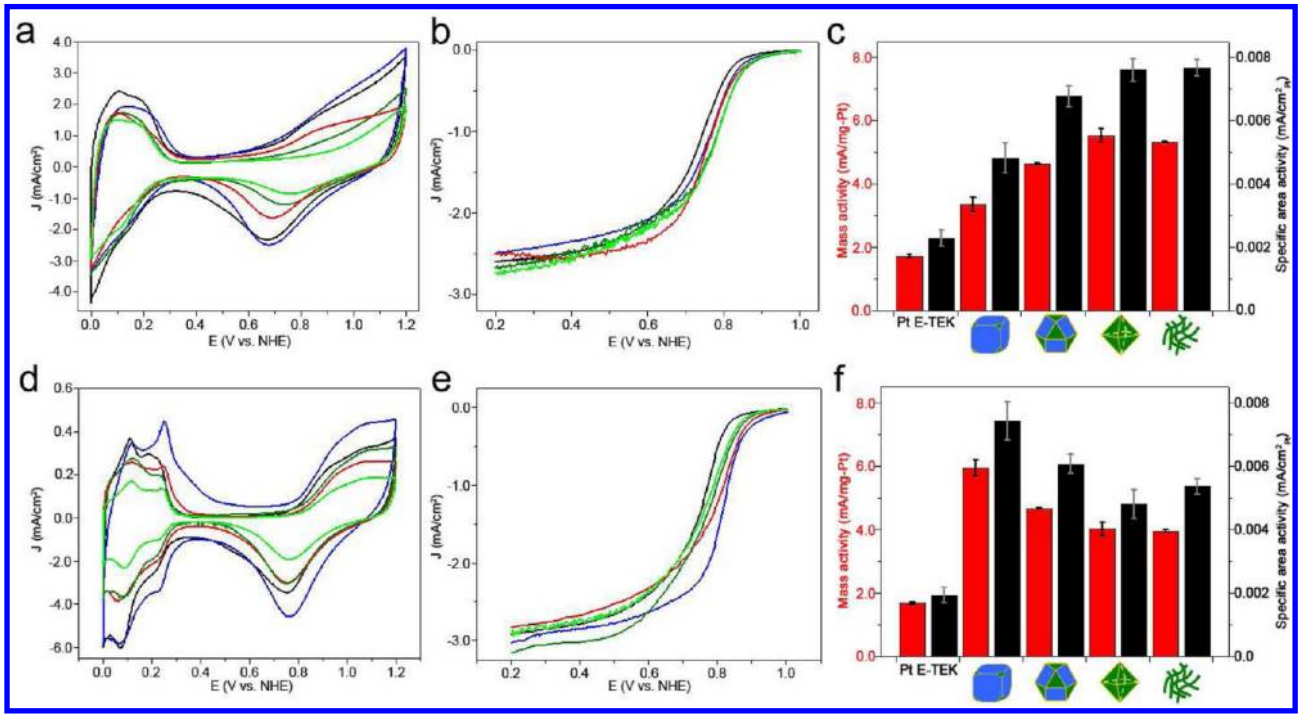

Figure 5. Cyclic voltammograms obtained in (a) 0.1 M $HClO_4$ and (d) 0.5 M H_2SO_4. ORR polarization curves of Pt E-TEK (black), nanocubes (blue), polyhedrons (red), octahedrons (green), and nanowires (light green) obtained in (b) 0.1 M $HClO_4$ and (e) 0.5 M H_2SO_4. MA (red column) and SA (black column) of different PtNiFe nanostructures performed in (c) 0.1 M $HClO_4$ and (f) 0.5 M H_2SO_4.

dx.doi.org/10.1021/cm301039a | *Chem. Mater.* 2012, 24, 2527–2533

octahedrons. The combination of these results clearly demonstrates the shape-sensitivity of the PtNiFe nanostructures in ORR.

Figure 5d–f shows the electrochemical measurements performed in H_2SO_4. The hydrogen desorption area, electric charge, active area, and specific area from CV curves are summarized in Table S2 (Supporting Information). Most importantly, the CV curve of PtNiFe nanocubes (Figure 5d) exhibits the highest signal of hydrogen desorption at ~0.25 V. Accordingly, the highest signal at ~0.25 V originates from the hydrogen desorption on the (100) facet of polycrystallines.[7b,20,21] Also, Figure 5e shows that the onset potentials of all PtNiFe nanocrystals are more positive than that of Pt E-TEK in the region of 0.8–1.0 V. The results of kinetic current densities (at 0.9 V) normalized to the effective Pt mass are obtained as shown in Figure 5c. The ORR MA for all samples is in the following sequence: nanocubes (5.94 ± 0.254 mA/mg-Pt) > polyhedrons (4.67 ± 0.021 mA/mg-Pt) > octahedrons (4.02 ± 0.205 mA/mg-Pt) > nanowires (3.95 ± 0.04 mA/mg-Pt) > Pt E-TEK (1.68 ± 0.056 mA/mg-Pt). Accordingly, the calculated SA for all types of catalysts are in the following sequence: nanocubes (0.0074 ± 0.00060 mA/cm^2_{Pt}) > polyhedrons (0.0061 ± 0.0003 mA/cm^2_{Pt}) > nanowires (0.0052 ± 0.00024 mA/cm^2_{Pt}) > octahedrons (0.0048 ± 0.00046 mA/cm^2_{Pt}) > Pt E-TEK (0.0019 ± 0.00025 mA/cm^2_{Pt}). Compared to the ORR activity between octahedron and polyhedron, the result reveals a reverse order in the ORR activities among the PtNiFe nanostructures (cf., Figure 5e and 5f in H_2SO_4). This opposite trend is expected and can be rationalized by the nature of the electrolytes. The higher performance in polyhedrons mainly stems from the weak adsorption of sulfate anion on the (100) planes of Pt-based alloy (Scheme 2).[6c,d,21,22] In particular, the superior ORR activities of PtNiFe nanocubes among these samples are highlighted. Despite the largest size and excessive Pt content, the exposure of the (100) plane in the nanocube is the highest among these nanostructures, rationalizing the outperformance of the ORR activities of nanocubes over those of polyhedrons, octahedrons, and nanowires. The sample-to-sample reproducibility in the presence of H_2SO_4 can be seen in Figure S8 (Supporting Information), and a reproducible trend of ORR enhancement has been consistently obtained. Clearly, the trend of ORR activity for PtNiFe nanostructures (Figure 5c and 5f) performed in different electrolytes is dependent on the shape but independent of the alloying composition and size. Finally, in the durability test, the nanocatalysis of PtNiFe nanocubes was performed in H_2SO_4 by cycling the potential between 0.0 and 1.2 V (vs NHE). Figure S9 (Supporting Information) shows the CV and polarization curves before and after the durability test. The almost overlapping polarization curves, shown in Figure S9b, indicate that there is no significant loss of MA and SA, with a decrease of ~6.8% and ~2%, respectively, after the durability test (see inset of Figure S9b).

Scheme 2. Adsorption of Bisulfate Anions on the (111) and (100) Planes of Pt-Based Alloy

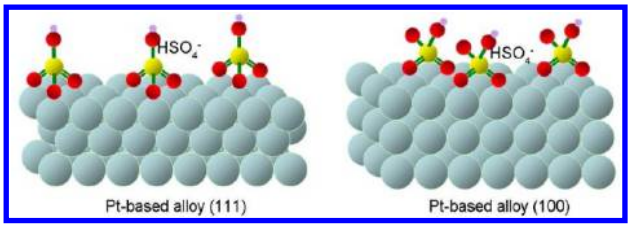

CONCLUSIONS

PtNiFe nanostructures with the various shapes of nanocube, polyhedron, octahedron, and nanowire are successfully prepared through the fine adjustments of crystal facet–surfactant bindings. In view of the ORR activities, all PtNiFe nanostructures have superior MA and SA over that of Pt E-TEK. Also, the shape dependency in the ORR activity of PtNiFe nanostructures is clearly unveiled. PtNiFe octahedrons and nanowires enclosed by {111} facets show higher MA and SA in $HClO_4$. In contrast, PtNiFe nanocubes enclosed by {100} facets show excellent MA and SA in H_2SO_4. Thus, the synthetic strategy for shape control of multialloy nanocrystals and the correlated catalytic activities presented in this study may provide an efficacy avenue for the preparation of highly performing nanocatalysts in fuel cells.

ASSOCIATED CONTENT

Supporting Information

TEM of nanostructures, size and length distribution, Table S1, Table S2, X-ray energy dispersive spectra, the repeatable results of ORR for all PtNiFe nanostructures in H_2SO_4 and alloying composition. This material is available free of charge via the Internet at http://pubs.acs.org.

AUTHOR INFORMATION

Corresponding Author

*E-mail: chop@ntu.edu.tw (P.-T.C.); cheny2@phys.sinica.edu.tw (Y.-Y.C.); t42005@ntnu.edu.tw (C.-C.C.).

Notes

The authors declare no competing financial interest.

ACKNOWLEDGMENTS

This work is supported by National Science Council, Taiwan. The authors thank Ching-Yen Lin, Ya-Yun Yang, and Chih-Yuan Tang in Instrumentation Center, National Taiwan University, for assistance in the obtainment and analysis of TEM images.

REFERENCES

(1) Steele, B. C. H.; Heinzel, A. *Nature* **2001**, *414*, 345.

(2) (a) Gasteiger, H. A.; Kocha, S. S.; Sompalli, B.; Wagner, F. T. *Appl. Catal., B* **2005**, *56*, 9. (b) Hamnett, A. *Catal. Today* **1997**, *38*, 445. (c) Peng, Z. M.; Yang, H. *Nano Today* **2009**, *4*, 143.

(3) (a) Chen, W.; Kim, J. M.; Sun, S. H.; Chen, S. W. *J. Phys. Chem. C* **2008**, *112*, 3891. (b) Paulus, U. A.; Wokaun, A.; Scherer, G. G.; Schmidt, T. J.; Stamenkovic, V.; Radmilovic, V.; Markovic, N. M.; Ross, P. N. *J. Phys. Chem. B* **2002**, *106*, 4181. (c) Markovic, N. M.; Schmidt, T. J.; Stamenkovic, V.; Ross, P. N. *Fuel Cells* **2001**, *1*, 105. (d) Yang, H. Z.; Zhang, J.; Kumar, S.; Zhang, H. J.; Yang, R. D.; Fang, J. Y.; Zou, S. Z. *Electrochem. Commun.* **2009**, *11*, 2278. (e) Wanjala, B. N.; Fang, B.; Luo, J.; Chen, Y. S.; Yin, J.; Engehard, M. H.; Loukrakpam, R.; Zhong, C. J. *J. Am. Chem. Soc.* **2011**, *133*, 12714. (f) Lim, B.; Jiang, M. J.; Camargo, P. H. C.; Cho, E. C.; Tao, J.; Lu, X. M.; Zhu, Y. M.; Xia, Y. N. *Science* **2009**, *324*, 1302. (g) Zhang, H.; Jin, M. S.; Wang, J. G.; Li, W. Y.; Camargo, P. H. C.; Kim, M. J.; Yang, D. R.; Xie, Z. X.; Xia, Y. N. *J. Am. Chem. Soc.* **2011**, *133*, 6078. (h) Wang, C.; Chi, M.; Wang, G.; Vliet, D. V. D.; Li, D.; More, K.; Wang, H.-H.; Schlueter, J. A.; Markovic, N. M.; Stamenkovic, V. R. *Adv. Funct. Mater.* **2011**, *21*, 147.

(4) (a) Jalan, V.; Taylor, E. J. *J. Electrochem. Soc.* **1983**, *130*, 2299. (b) Mukerjee, S.; Srinivasan, S.; Soriaga, M. P.; Mcbreen, J. *J.*

Electrochem. Soc. **1995**, *142*, 1409. (c) Mukerjee, S.; Srinivasan, S.; Soriaga, M. P.; Mcbreen, J. *J. Phys. Chem.* **1995**, *99*, 4577. (d) Stamenkovic, V.; Schmidt, T. J.; Ross, P. N.; Markovic, N. M. *J. Phys. Chem. B* **2002**, *106*, 11970.
(5) (a) Stamenkovic, V. R.; Mun, B. S.; Arenz, M.; Mayrhofer, K. J. J.; Lucas, C. A.; Wang, G. F.; Ross, P. N.; Markovic, N. M. *Nat. Mater.* **2007**, *6*, 241. (b) Toda, T.; Igarashi, H.; Uchida, H.; Watanabe, M. *J. Electrochem. Soc.* **1999**, *146*, 3750. (c) Stamenkovic, V. R.; Fowler, B.; Mun, B. S.; Wang, G. F.; Ross, P. N.; Lucas, C. A.; Markovic, N. M. *Science* **2007**, *315*, 493.
(6) (a) Wu, J. B.; Yang, H. *Nano Res.* **2011**, *4*, 72. (b) Wu, J. B.; Zhang, J. L.; Peng, Z. M.; Yang, S. C.; Wagner, F. T.; Yang, H. *J. Am. Chem. Soc.* **2010**, *132*, 4984. (c) Choi, S. I.; Choi, R.; Han, S. W.; Park, J. T. *Chem. Commun.* **2010**, *46*, 4950. (d) Choi, S. I.; Choi, R.; Han, S. W.; Park, J. T. *Chem.—Eur. J.* **2011**, *17*, 12280. (e) Kang, Y. J.; Murray, C. B. *J. Am. Chem. Soc.* **2010**, *132*, 7568.
(7) (a) Zhang, J.; Fang, J. Y. *J. Am. Chem. Soc.* **2009**, *131*, 18543. (b) Zhang, J.; Yang, H. Z.; Fang, J. Y.; Zou, S. Z. *Nano Lett.* **2010**, *10*, 638.
(8) Wu, J. B.; Gross, A.; Yang, H. *Nano Lett.* **2011**, *11*, 798.
(9) (a) Yin, Y.; Alivisatos, A. P. *Nature* **2005**, *437*, 664. (b) Chou, S. W.; Zhu, C. L.; Neeleshwar, S.; Chen, C. L.; Chen, Y. Y.; Chen, C. C. *Chem. Mater.* **2009**, *21*, 4955. (c) Mokari, T. L.; Zhang, M. J.; Yang, P. D. *J. Am. Chem. Soc.* **2007**, *129*, 9864. (d) Tao, A. R.; Habas, S.; Yang, P. D. *Small* **2008**, *4*, 310.
(10) Ferrando, R.; Jellinek, J.; Johnston, R. L. *Chem. Rev.* **2008**, *108*, 845.
(11) Liu, Q. S.; Yan, Z.; Henderson, N. L.; Bauer, J. C.; Goodman, D. W.; Batteas, J. D.; Schaak, R. E. *J. Am. Chem. Soc.* **2009**, *131*, 5720.
(12) Klug, H. P.; Alexander, L. E. *X-ray Diffraction Procedures for Polycrystalline and Amorphous Materials*; Wiley: New York, 1962.
(13) (a) Chen, M.; Pica, T.; Jiang, Y. B.; Li, P.; Yano, K.; Liu, J. P.; Datye, A. K.; Fan, H. Y. *J. Am. Chem. Soc.* **2007**, *129*, 6348. (b) Wang, C.; Hou, Y. L.; Kim, J. M.; Sun, S. H. *Angew. Chem., Int. Ed.* **2007**, *46*, 6333.
(14) Wulff, G. Z. *Kristallogr.* **1901**, *34*, 449.
(15) (a) Wang, Z. L. *J. Phys. Chem. B* **2000**, *104*, 1153. (b) Xia, Y. N.; Xiong, Y. J.; Lim, B.; Skrabalak, S. E. *Angew. Chem., Int. Ed.* **2009**, *48*, 60.
(16) (a) Jun, Y. W.; Choi, J. S.; Cheon, J. *Angew. Chem., Int. Ed.* **2006**, *45*, 3414. (b) Xia, X. H.; Zeng, J.; Oetjen, L. K.; Li, Q.; Xia, Y. N. *J. Am. Chem. Soc.* **2012**, *134*, 1793. (c) Bealing, C. R.; Baumgardner, W. J.; Choi, J. J.; Hanrath, T.; Hennig, R. G. *ACS Nano* **2012**, *6* (3), 2118–2127.
(17) Zeng, J.; Zheng, Y. Q.; Rycenga, M.; Tao, J.; Li, Z. Y.; Zhang, Q. A.; Zhu, Y. M.; Xia, Y. N. *J. Am. Chem. Soc.* **2010**, *132*, 8552.
(18) (a) Aliaga, C.; Park, J. Y.; Yamada, Y.; Lee, H. S.; Tsung, C. K.; Yang, P. D.; Somorjai, G. A. *J. Phys. Chem. C* **2009**, *113*, 6150. (b) Vidal-Iglesias, F. J.; Solla-Gullon, J.; Herrero, E.; Montiel, V.; Aldaz, A.; Feliu, J. M. *Electrochem. Commun.* **2011**, *13*, 502.
(19) Shao, M. H.; Yu, T.; Odell, J. H.; Jin, M. S.; Xia, Y. N. *Chem. Commun.* **2011**, *47*, 6566.
(20) Wang, C.; Daimon, H.; Lee, Y.; Kim, J.; Sun, S. *J. Am. Chem. Soc.* **2007**, *129*, 6974.
(21) Wang, C.; Daimon, H.; Onodera, T.; Koda, T.; Sun, S. H. *Angew. Chem., Int. Ed.* **2008**, *47*, 3588.
(22) (a) Sanchez-Sanchez, C. M.; Solla-Gullon, J.; Vidal-Iglesias, F. J.; Aldaz, A.; Montiel, V.; Herrero, E. *J. Am. Chem. Soc.* **2010**, *132*, 5622. (b) Mostany, J.; Herrero, E.; Feliu, J. M.; Lipkowski, J. *J. Phys. Chem. B* **2002**, *106*, 12787.